Title

Adsorption and reduction of roxarsone on magnetic greigite (Fe3S4): Indispensable role of structural sulfide

Permalink

Authors

Liu, Wei
Ai, Zhihui
Dahlgren, Randy A
et al.

Publication Date

DOI

Peer reviewed

Adsorption and reduction of roxarsone on magnetic greigite (Fe$_3$S$_4$): Indispensable role of structural sulfide

Wei Liu[a,b], Zhihui Ai[b], Randy A. Dahlgren[a], Lizhi Zhang[b,*], Xuedong Wang[a,*]

[a] *Key Laboratory of Watershed Sciences and Health of Zhejiang Province, Wenzhou Medical University, Wenzhou 325035, People's Republic of China*
[b] *Key Laboratory of Pesticide & Chemical Biology of Ministry of Education, Institute of Environmental Chemistry, College of Chemistry, Central China Normal University, Wuhan 430079, People's Republic of China*

GRAPHICAL ABSTRACT
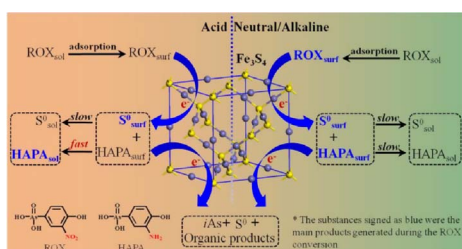
ABSTRACT

Roxarsone (ROX) is an organoarsenic compound that is widely used as an additive in swine and poultry feed to inhibit disease and promote growth. Due to its low metabolism in animals, it is excreted in animal urine and feces leading to its widespread contamination of soils and aquatic ecosystems. Herein, we demonstrated that ROX can be adsorbed and subsequently reduced by a common iron sulfide (greigite - Fe$_3$S$_4$) in the pH range of 3.6 to 8.6. ROX removal processes followed a pseudo-second-order kinetic model that was strongly pH dependent. The nitro group of ROX was reduced by structural sulfide rather than dissolved sulfide or ferrous iron to generate an amino-group containing product, 4-hydroxy-3-aminophenylarsonic acid (HAPA). At neutral to alkaline pH values ROX and HAPA are preferentially adsorbed rather than reduced on the Fe$_3$S$_4$ surface. The interaction between ROX and Fe$_3$S$_4$ was minimally affected by interactions with coexisting cations, anions and natural organic matter (humic acid). These novel findings provide new insights for understanding the transformation mechanism of ROX by iron sulfides minerals, and have practical application for designing efficient systems for advanced treatment of ROX.

1. Introduction

Organoarsenic compounds, such as roxarsone (ROX, 4-hydroxy-3-nitrophenylarsonic acid) and *p*-arsanilic acid (*p*-ASA, 4-aminophenylarsonic acid), have been widely used since the 1960s as additives in swine and poultry feed to inhibit diseases and promote growth [1]. Due to their low metabolism in livestock, organoarsenic additives are excreted relatively unchanged in animal urine and feces. The organoarsenic compounds are readily leached from manures and soils due to their high water solubility leading to their prevalence in both terrestrial and aquatic ecosystems [2,3]. Arsenic concentrations in chicken and swine manure are reported as high as 0.6–43.8 and 0.42–119.0 mg/kg, respectively [4]. Moreover, organoarsenic additives may be converted to more mobile and toxic inorganic arsenic species by microbial

transformations, which subsequently enhance their environmental risk. Hence, the European Union and United States banned the use of ROX and *p*-ASA as animal feed additives in 1999 and 2013, respectively [5]. However, these organoarsenic feed additives are still widely used in many developing countries around the word, such as China, India and Brazil [4]. As a consequence, their safety has raised great concern to human and environmental health in these countries.

Organoarsenic conversion induced by waterborne particles, river sediments and soil minerals is an important way for its abiotic transformation in the natural environment. Recently, iron (oxyhydr)oxides [6], multi-walled carbon nanotubes [7], anaerobic granular sludge [8], and specific modified particles [9–11] are often used as adsorbent to investigate the organoarsenic fate mediated by natural particles. Its adsorption mechanisms involve surface complex, electrostatic interactions and so on [12–14]. Although organoarsenic adsorption with natural particles is not realized its structural transformation, the abiotic processing is regarded as a prerequisite for organoarsenic decomposition [15,16]. For example, Cheng et al. investigated *p*-ASA transformations on birnessite (δ-MnO_2), and found that *p*-ASA was efficiently degraded via the formation of *p*-ASA radicals through single-electron transfer to δ-MnO_2 and subsequent cleavage of the C-As bond [17]. Jiang and coworkers. utilized spent aluminum beverage cans to activate molecular oxygen and generate hydrogen peroxide, which was subsequently decomposed by ferrous ions to produce hydroxyl radicals for *p*-ASA degradation. The Al(III) ions were also an excellent flocculent for inorganic arsenic removal [18]. All of these processes mediated the organoarsenic adsorption or/and redox, however, its transformation pathway was strongly dependent on natural particles.

Due to the specificity and complexity of the natural environment, the ambient conditions such as solution pH, coexist ions, ionic strength and the interface properties of natural particles may also play an important role in the organoarsenic transformation. For example, Chen and co-workers found that Fe^{3+}, Zn^{2+} and Cu^{2+} dramatically enhanced the ROX adsorption on goethite surface, however, PO_4^{2-} was competitively adsorbed on the surface of iron minerals leading to organoarsenic desorption [19]. Hu et al., found that the solution pH could affect the ROX removal efficiency by Fe/La-modified montmorillonite via mediate the degree of ionization, speciation of ionizable chemicals, and surface charge of adsorbents [20]. Jhung et. al. reported that the mesoporos zeolitic imidazolate framework-8 could adsorptively remove *p*-ASA via electrostatic interactions and its adsorption kinetics and adsorbed amount were improved with mesoporosity [21]. Their subsequent study proved that hydroxyl group functionalized MOFs (MIL-101-$(OH)_3$) could directly define H-donor for the formation of H-bound between *p*-ASA and MOFs, which extremely promoted the *p*-ASA adsorption on MIL-101-$(OH)_3$ [22]. In addition, the surface defect on the particles could also act as an activate site for the organoarsenic effective adsorption [23]. All of these studies reveal that the interaction between the organoarsenic and minerals is closely dependent on ambient conditions and natural particle properties, which provided a critical pathway for organoarsenic transformation in the natural environment.

Iron sulfides, an abundant Earth mineral with high ferrous and sulfide contents, play an important role in the global cycles of carbon, oxygen, sulfur and other elements [24–26]. Recent studies have examined the efficacy of using iron sulfides as an adsorbent and/or reductant for remediation of chlorinated organic compounds, nitrate, and metal ions [27–31]. Among the various iron sulfides, greigite (Fe_3S_4) has drawn particular attention as it contains both ferrous and ferric ions and has excellent magnetic properties [24]. For example, Fe_3S_4 has been used as an anode material for ion batteries and as a reductant for CO_2 conversion to small organic molecules due to its excellent reductive properties, and as an adsorbent for Pb(II) and dyes owing to its complex functional group surface chemistry [25,32–35]. However, there is a paucity of information on the reaction mechanisms between magnetic Fe_3S_4 and organic compounds, especially organoarsenic utilized for livestock feed additives.

Based on the above considerations, this investigation focuses on ROX adsorption and reduction mechanism induced by solovthermally synthesized magnetic Fe_3S_4 nanosheets. A series of experiments were conducted to investigate the generation of reactive species and their effects on ROX transformations. High performance liquid chromatography (HPLC) and atomic fluorescence spectrometry (AFS) were used to identify intermediate ROX reduction products and elucidate ROX removal mechanisms. This study provides new insights for understanding the transformation mechanism of ROX by iron sulfides minerals and has application for designing efficient systems for advanced treatment of ROX in the environment.

2. Material and methods

2.1. Chemicals

Analytical grade iron(III) chloride hexahydrate ($FeCl_3 \cdot 6H_2O$), sodium chloride, potassium chloride, magnesium chloride, calcium chloride, sodium sulfate, sodium nitrate, thiourea, sulfur powder, carbon disulfide, oxalic acid dihydrate, potassium borohydride, ascorbic acid, hydrochloric acid, and ethylene glycol (EG) were purchased from National Medicines Co. (Shanghai, China). Roxarsone (ROX, 98%) and humic acid (HA, 98%) were purchased from J & K Scientific (Beijing, China). 4-Hydroxy-3-aminophenylarsonic acid (HAPA, 98%) was purchased from BOC Sciences (Shirley, NY, USA). The molecular structures of ROX and HAPA are illustrated in Fig. S1. $NaAsO_2$, $NaAsO_3$ and 2, 2, 6, 6-tetramethylpiperidinooxy (TEMPO) and HPLC-grade phosphoric acid, formic acid and acetic acid were purchased from Sigma-Aldrich (St. Louis, MO, USA). Chromatographic-grade methanol and acetonitrile were obtained from Merck KGaA (Darmstadt, Germany). All chemicals were used as received without further purification. Deionized water (> 18 MΩ) was used throughout the experiments.

2.2. Sample preparation

In a typical Fe_3S_4 synthesis [36], $FeCl_3 \cdot 6H_2O$ (3.0 mmol) and thiourea (6.0 mmol) were dissolved in 60 mL of EG to form a carmine solution under magnetic stirring. The solution was then transferred into a 100 mL Teflon-lined stainless steel autoclave, which was sealed and heated at 180 °C for 12 h in an electrical oven. Following completion of the heating step, the autoclave was cooled to room temperature. Finally, the dark solid product (Fe_3S_4) was obtained by centrifugation and sequential rinsing with distilled water and ethanol before drying in a vacuum oven at 60 °C for 4 h.

2.3. Experimental procedures

A stock solution containing of 500 mg/L of ROX was prepared by dissolving ROX in deionized water with subsequent storage in the dark to avoid photochemical degradation. Simulated wastewaters with different ROX concentrations (1.0–40.0 mg/L) were prepared by dilution of the stock ROX standard solution with deionized water. The pH values were measured with an Orion model 920A pH/ISE meter and Beckman combination electrode. The initial pH of the ROX (10 mg/L) solution was 4.6; additional pH values were prepared by addition of 0.1 mol/L HCl or 0.1 mol/L NaOH.

ROX removal experiments were conducted in 50 mL conical flasks containing 20 mL of ROX and 0.5 g/L of Fe_3S_4. Each flask was covered with aluminum foil (to shield from light) and mixed with a rotary shaker at a constant temperature of 30 °C. To explore solution matrix effects, the ROX removal experiments were also carried out with the addition of 1 mmol/L of various inorganic salts (including NaCl, KCl, $MgCl_2$, $CaCl_2$, Na_2SO_4, $NaNO_3$,) and 10 mg/L of natural organic matter (humic acid). Sub-samples were withdrawn from the flask with a syringe at a regular time interval and passed through a 0.22 μm
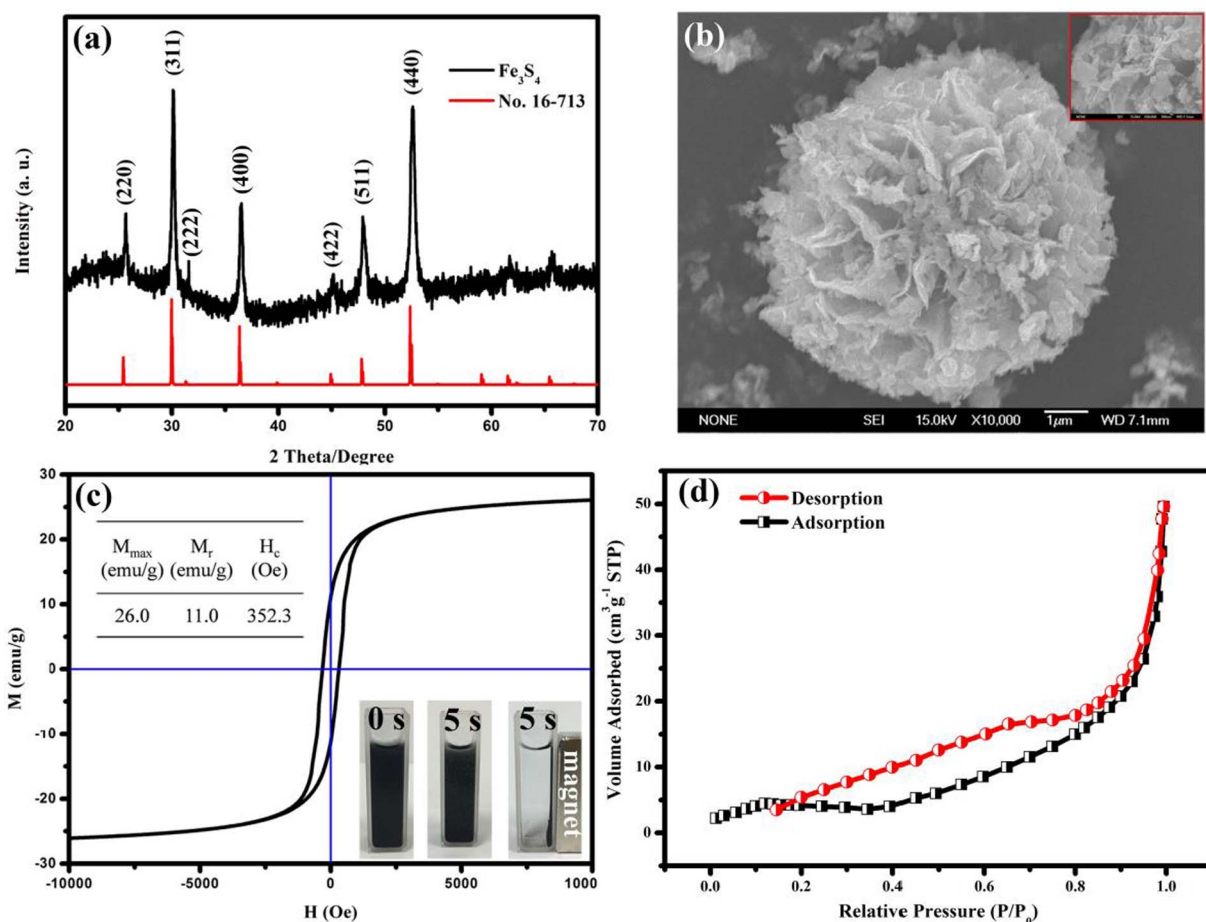
Fig. 1. Characterizations of solvothermal synthesized Fe_3S_4: (a) XRD; (b) SEM; (c) M-H curves, insert photographs show that Fe_3S_4 nanosheets were dispersed in water (left), and standing with/without a magnet after 5 s (middle and right); and (d) nitrogen adsorption-desorption isotherm.

polytetrafluoroethylene filter. The concentration of ROX was analyzed by HPLC for each time interval. All ROX removal experiments were conducted in triplicate.

2.4. Analytical methods

Concentrations of ROX and HAPA were determined by high performance liquid chromatography (HPLC, Ultimate 3000, Thermo, USA) with a photo diode array detector. Elemental sulfur adsorbed on Fe_3S_4 was extracted with methanol and analyzed by HPLC. The low molecular weight organic acids and inorganic anions were quantified by ion chromatography (Dionex 900; Thermo, Fremont, CA, USA). Inorganic arsenic (As(III) and As(V)) concentrations were determined by a combination of liquid chromatography (LC) and atomic fluorescence spectrometry (AFS 9600, Beijing Kechuang Haiguang Instrument Co., Beijing, China). The arsenic species were separated using a 250 × 4.1 mm Hamilton PRP X-100 anion-exchange column at 30 °C with an isocratic elution of 5 mmol/L Na_2HPO_4 and 45 mmol/L KH_2PO_4 buffer solution at 2.0 mL/min. Hydride generation of volatile arsines was conducted by adding online solutions of 5% HCl and 2% KBH_4 using a peristaltic pump with flow rates of 7 mL/min and 4 mL/min, respectively.

Electron spin resonance (ESR) spectra were obtained with a Bruker EPR A300 spectrometer (Bruker, Billerica, MA) at ambient conditions using TEMPO as the radical spin-trap reagent. X-ray diffraction (XRD) patterns in the range of 20° and 70° (2θ values) were obtained using a Bruker D8 Advance X-ray diffractometer with Cu Kα radiation. Scanning electron microscopy (SEM) was performed on a LEO 1450VP scanning electron microscope (Zeiss, Oberkochen, Germany). The

magnetic properties of the as-prepared Fe_3S_4 powder were determined at 298 K with a vibrating sample magnetometer (VSM-7300, Quantum Design, San Diego, CA, USA). Typical magnetic hysteresis loops were measured by sweeping the external field between −10 and 10 kOe. Nitrogen adsorption and desorption isotherms at 77 K were measured using a Micromeritics ASAP 2460 system (Micromeritics Instrument Corp., Norcross, GA, USA) following vacuum drying at 473 K overnight. The electron transfer ability of the magnetic Fe_3S_4 was evaluated by its free corrosion potentials via Tafel analysis. Tafel curves were determined with a CHI-660C electrochemical workstation (CH Instruments, Austin, TX, USA) employing a three electrode system of Fe_3S_4, platinum and standard hydrogen electrode as the work electrode (WE), counter electrode (CE) and reference electrode (RE), respectively. A 5 cm of length of cylindrical iron (Φ = 5 mm) was fixed in a Teflon tube holder to fabricate the work electrode. Prior to fabrication, the cylindrical iron surface was polished with emery paper. A 5 mg Fe_3S_4 sample was ground and applied to cover the end of the cylindrical iron, leaving only the surface exposed to 50 mL of 50 mmol/L Na_2SO_4 electrolyte in a 100 mL beaker. To measure the initial corrosion rates of Fe_3S_4, Tafel scans were acquired as soon as the work electrode was exposed to the solution. All Tafel diagrams were obtained by polarizing the work electrode at ± 200 mV with respect to its open circuit potential. To investigate pH effects on Fe_3S_4 corrosion rates, the electrochemical experiments were conducted across the pH range of 3.6 to 8.6 following pH adjustment by either 0.1 mol/L HCl or 0.1 mol/L NaOH. All potentials in the Tafel diagrams are reported with respect to the standard hydrogen electrode.

3. Results and discussion

3.1. Greigite (Fe₃S₄) characterization

The crystallographic phase and purity of the solvothermal synthesized Fe_3S_4 sample were examined by XRD characterization. The diffraction peaks were fully consistent with cubic greigite Fe_3S_4 (Joint Committee on Powder Diffraction Standards (JCPDS) Powder Diffraction File (PDF) No. 16-713) and demonstrated well indexed (2 2 0), (3 1 1), (2 2 2), (4 0 0), (4 2 2), (5 1 1) and (4 4 0) reflections in order of ascending 2θ values (Fig. 1a). No other impurities were detected in the diffraction patterns, indicating high phase purity of the as-synthesized powder at the XRD detection level. The broad, but sharp XRD diffraction peaks are consistent with the small crystallite size and high crystallinity of the Fe_3S_4 phase. SEM examination of the morphology and microstructure revealed large-scale, uniform nanosheets, which tended to form 3D flower-like microsphere aggregates (Fig. 1b).

The magnetic properties of the Fe_3S_4 nanosheets were recorded by a VSM device. The curves displayed a small hysteresis loop, and the saturation magnetization (*Ms*), remnant magnetization (*Mr*), and coercivity field (*Hc*) at room temperature were 26.0 emu/g, 11.0 emu/g and 352.3 Oe, respectively (Fig. 1c). The Fe_3S_4 powder was well dispersed in water forming a black suspension that could be rapidly collected by a magnet without any remaining residues in the solution after 5 s (Fig. 1c inset). These results demonstrate that the Fe_3S_4 can be quickly and efficiently separated from the suspension system with an external magnetic field.

Specific surface area of the Fe_3S_4 nanosheets was measured by the nitrogen adsorption-desorption method. A distinct hysteresis loop was observed at a relative pressure of 0.2–0.9 in the N_2 adsorption isotherm, which can be assigned as a type IV isotherm with H3-type hysteresis loops, indicating the presence of mesopores (Fig. 1d). The Brunauer - Emmett - Teller (BET) surface area calculated from the N_2 isotherm at 77 K was 13 m²/g. The specific surface area and porous nature of the magnetic Fe_3S_4 nanosheets significantly shortens ion diffusion lengths and provides more active sites for organic compound transformations, which may considerably enhance interactions between organic compounds and the Fe_3S_4 nanosheets.

3.2. Removal of ROX with Fe₃S₄ nanosheets

ROX removal kinetics by 0.5 g/L of Fe_3S_4 at different initial ROX concentrations at 30 °C were evaluated over time (Fig. 2a). Within 240 min, ROX concentration decreased by almost 100% and 60% at initial concentrations of 1 to 10 mg/L and 30 mg/L, respectively. This revealed that ROX was efficiently removed by the Fe_3S_4 nanosheets. The kinetics of ROX removal were evaluated in terms of pseudo-first-order and pseudo-second-order kinetic models by calculating removal constants (*k*), P values, and correlation coefficients (R^2) (Table S1). At initial concentrations of 1–6 mg/L, the *k* and R^2 were not determined due to the very rapid removal of ROX by the Fe_3S_4. The P values for pseudo-first-order and pseudo-second-order kinetic models were much lower than 0.001, suggesting the high significance level of the data for the fitting process. Moreover, the R^2 value for the pseudo-second-order model was much higher than that of the pseudo-first-order kinetic model at initial ROX concentrations of 8 to 30 mg/L (Table S1 and Fig. 2b), suggesting a better fit with the pseudo-second-order kinetic model. The pseudo-second-order rate constants slightly increased from 4.774 ± 0.373 to 4.872 ± 0.341 L·mmol⁻¹·min⁻¹ with increasing ROX concentrations from 8 to 10 mg/L, and then sharply decreased to 0.058 ± 0.004 L·mmol⁻¹·min⁻¹ with a further increase in ROX concentration from 10 to 30 mg/L. Given that the ROX removal efficiency was highly dependent on its initial concentration, 10 mg/L ROX was selected for subsequent investigations examining ROX removal mechanism(s).

3.3. Matrix effects on ROX removal by Fe₃S₄ nanosheets

As ROX and Fe_3S_4 may simultaneously exist in natural terrestrial and aquatic environments, ROX transformation based on Fe_3S_4 could be an important organoarsenic conversion pathway. However, in natural environments several anions, cations and natural organic compounds coexist and may interact with the reactions between ROX and Fe_3S_4. Therefore, a variety of coexisting ions and a humic substance were evaluated for their effects on the removal efficiency of ROX by Fe_3S_4. The ROX removal efficiencies for all ions (Na^+, K^+, Mg^{2+}, Ca^{2+}, Cl^-, SO_4^{2-} and NO_3^-) and HA evaluated were 99 + % indicating no significant matrix effects from these constituents on ROX removal (Fig. S2).

3.4. pH effects on ROX removal by Fe₃S₄ nanosheets

Organoarsenic compounds maybe removed via adsorption and/or redox pathways with heterogeneous materials. Because adsorption and redox processes are pH dependent, the effect of pH on ROX removal efficiency by Fe_3S_4 was evaluated. More than 90% of the ROX was removed by the Fe_3S_4 nanosheets in the initial pH range of 3.6 to 8.6 (Fig. 3a). The apparent ROX removal rate constants slightly increased from 4.557 ± 0.658 to 4.872 ± 0.341 L·mmol⁻¹·min⁻¹ with increasing pH from 3.6 to 4.6, but sharply decreased to 0.832 ± 0.017 L·mmol⁻¹·min⁻¹ when the initial pH was increased to 8.6 (Table S2). To clarify the contribution of adsorption and redox processes on ROX removal by Fe_3S_4, the probable organic intermediates (e.g., HAPA & inorganic As species) generated during the ROX removal process were investigated using HPLC. HAPA was generated during the ROX removal process in the pH range of 3.6–8.6 (Fig. 3b), revealing that the $-NO_2$ moiety of ROX was reduced by the Fe_3S_4 to generate $-NH_2$. HAPA concentrations increased with increasing reaction time, suggesting a high stability of HAPA in these systems. However, the final HAPA concentration decreased from 7.50 to 3.16 mg/L when the initial pH was increase from 3.6 to 8.6, indicating that the nitro-group reduction process was highly pH dependent and/or preferential adsorption of HAPA on the Fe_3S_4 at high pH values.

Total inorganic arsenic species (denoted as *i*As, including inorganic As(III) and As(V)) were quantified to evaluate the possible breakage of the C-As bond in ROX during the reduction process. Dissolved *i*As concentrations quickly increased in the initial pH range of 3.6–8.6 and reached a maximum level after 20–30 min, followed by decreased concentrations with further reaction time (Fig. 3c). Moreover, dissolved iAs concentrations under acidic conditions were lower than those at neutral and alkaline conditions. This may result from more efficient reduction of $-NO_2$ at the expense of C-As at the higher proton concentrations. However, maximum inorganic arsenic concentrations were only ~70 μg/L, which were much lower than the initial total arsenic concentration calculated in ROX (2.85 mg/L). Thus, the breakage of the C-As bond was revealed as a minor process during ROX conversion by Fe_3S_4 nanosheets.

Total dissolved As concentrations were calculated as the sum of ROX, HAPA and inorganic arsenic (Fig. 3d). Total dissolved As concentrations at pH 8.6 were much lower than for neutral and acidic solutions; ROX conversion efficiency and HAPA generation efficiency were also slower at the higher pH value. These results revealed that the lower pH was favorable to the reduction of ROX, while the neutral and alkaline conditions enhanced adsorption of ROX and HAPA.

To confirm the reduction of $-NO_2$ to $-NH_2$ via reaction with Fe_3S_4 nanosheets, the reaction of nitrobenzene (NB) and Fe_3S_4 was carried out under conditions identical to the ROX- Fe_3S_4 reactions. NB concentration decreased with increasing reaction time and 65% of the NB was removed after 240 min (Fig. S3). Meanwhile, aniline (AN) was detected and quantified by HPLC analysis. The concentration of AN gradually increased from 0 to 0.03 mg/L with increasing reaction time, which confirmed $-NO_2$ reduction and $-NH_2$ generation by interaction
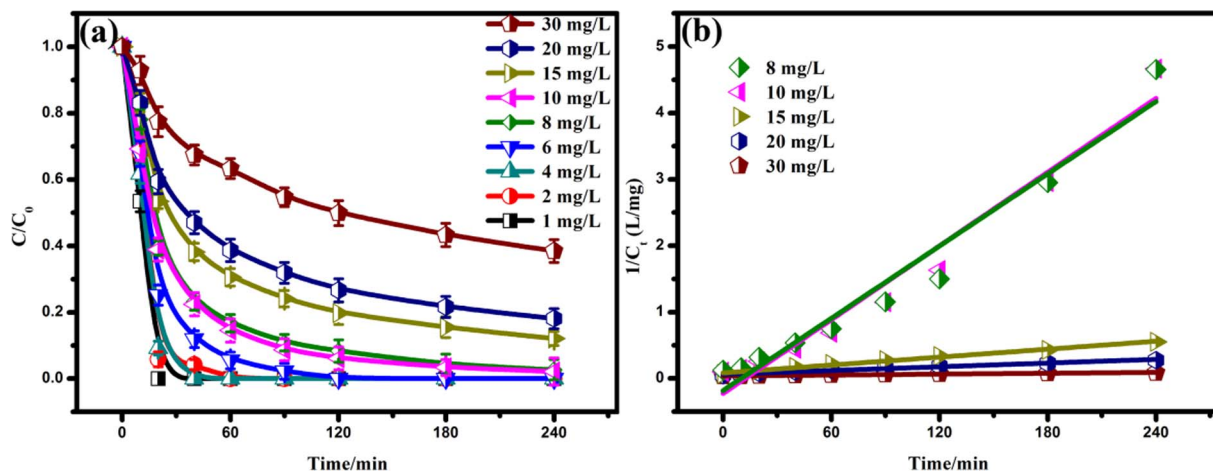
Fig. 2. (a) Time profiles for ROX removal with different initial ROX concentrations. (b) Plots of $1/C_t$ versus time for ROX removal. The concentration of Fe_3S_4 was 0.5 g/L and the initial ROX concentration increased from 1 to 30 mg/L. The initial pH of the systems was 4.6.

with Fe_3S_4. However, total N concentration, including NB and AN, was slightly decreased during the NB transformation process, possibly resulting from adsorption of NB and/or AN on Fe_3S_4 surfaces. In total, these results confirm the reduction ability of Fe_3S_4 nanosheets for the conversion of $-NO_2$ to $-NH_2$.

As the reduction of ROX to HAPA involves transfers of both electrons and protons, the effects of pH on the electron transfer properties of Fe_3S_4 were subsequently investigated. Specifically, corrosion potentials for Fe_3S_4 in the presence of 10 mg/L of ROX across the initial pH range of 3.6 to 8.6 were measured using Tafel polarization diagrams. The free corrosion potentials for magnetic Fe_3S_4 decreased from -0.61 to -0.69 V as the initial pH value increased from 3.6 to 8.6 (Fig. 4a). As more negative free corrosion potential values reflect higher electron transfer rates, it can be concluded that the lower pH enhanced the reduction of ROX to generate HAPA. These results confirm that the reduction of ROX is dependent on the electron transfer ability of Fe_3S_4 and protons.

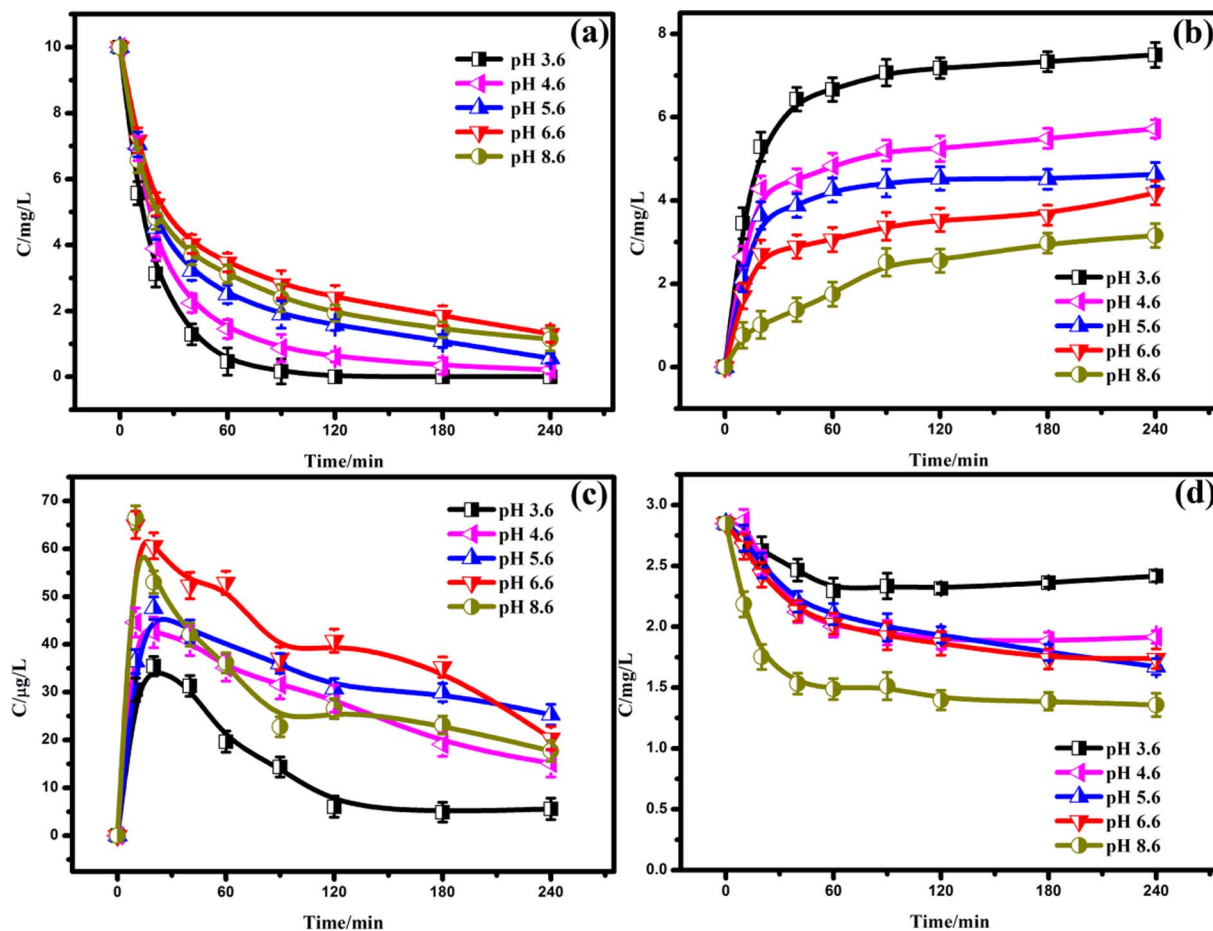**Fig. 3.** Time profiles for ROX, HAPA, iAs and total As with Fe_3S_4 at initial pH values of 3.6–8.6: (a) ROX; (B) HAPA; (c) iAs and (d) total As. The concentrations of Fe_3S_4 and ROX were 0.5 g/L and 10 mg/L, respectively.
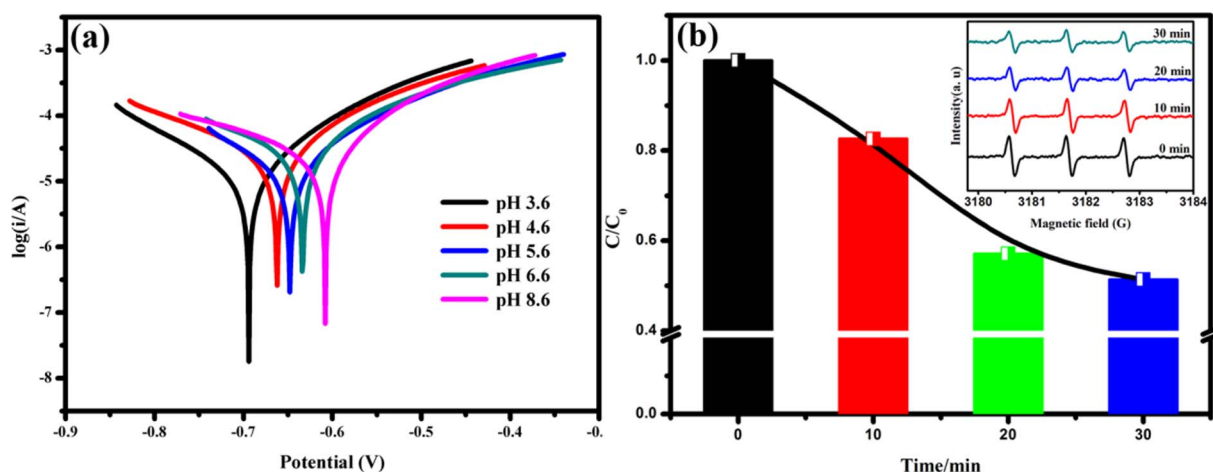
Fig. 4. (a) Tafel scans in the presence of Fe_3S_4 at initial pH values of 3.6–8.6; (b) Time profile of the ESR signal intensity of TEMPO, the inset shows the ESR spectra of TEMPO at 0–30 min. The concentration of Fe_3S_4 and TEMPO were 0.5 g/L and 5 mmol/L, respectively.

3.5. Electron transfer mechanisms for ROX reduction by Fe_3S_4 nanosheets

To confirm the electron transfer from the Fe_3S_4 nanosheets to ROX, electron spin resonance (ESR) spectra were used to identify electron (e^-) transfer with TEMPO as the radical spin-trap reagent. TEMPO is a typical spin label molecule that has a stable triplet ESR spectrum, however, it can be reduced by e^- to generate hydroxylamine (TEMPOH), which weakens the ESR signal [37]. The generation of e^- and their reactivity can be easily monitored by comparing changes in the ESR spectrum of TEMPO. A typical triplet peak with intensities of 1:1:1 was observed without addition of magnetic Fe_3S_4 indicating no electron transfer (Fig. 4b). However, the peak signal significantly decreased with increasing contact time, which was concomitant with the disappearance of 49% of the TEMPO (Fig. 4b). To clarify the effects of direct adsorption contribution on the decrease of TEMPO signals, Cr(VI) was used as electron scavengers to inhibit the reaction between TEMPO and electrons [38,39]. It was found that only 6% of TEMPO diminished in the presence of excess of Cr(VI), suggested the preferentially reaction between electrons and Cr(VI) rather than TEMPO (Fig. S4). These results indirectly ruled out the TEMPO adsorption on the Fe_3S_4 and confirmed that Fe_3S_4 efficiently generates e^- for the reduction of ROX.

Iron sulfides have the ability to reduce heavy metals and halogenated and nitro organic compounds due to the strong reducing capacity of sulfide and ferrous ions. To clarify the specific electron donors involved in ROX reduction by Fe_3S_4 nanosheets, 2,2′-bipyridine (BPY) was added to complex the ferrous ion allowing for an estimate of its reduction contribution to ROX removal. ROX removal efficiency in the presence of BPY was consistent with that in the absence of BPY (Fig. 5a), ruling out the role of ferrous ions on ROX reduction. Accordingly, it implies that the low valence sulfide plays the dominant role in ROX reduction. Hence, the probable oxidation products of

sulfide oxidation (e.g., elemental S^0 & SO_4^{2-}) were monitored during ROX reaction with Fe_3S_4. Most strikingly, elemental sulfur instead of sulfur-containing ions was detected by HPLC and IC analyses during ROX removal by Fe_3S_4 (Fig. 5b). Based on these results, we conclude that ROX was mainly reduced by sulfide rather than ferrous ions. However, the maximum elemental sulfur concentration was only 0.2 mg/L in solution, which was much lower than expected from the total amount of ROX reduction. This phenomenon might result from the strong hydrophobicity of elemental sulfur limiting its solubility, and thus elemental sulfur analysis was performed on ethanol extracts from the Fe_3S_4 surface following the reduction process. As inferred, the elemental sulfur concentration extracted from Fe_3S_4 surfaces was much higher than in solution (Fig. 5c). Collectively, these data confirmed that ROX reduction is primarily mitigated by sulfide originating from the Fe_3S_4 surface.

Given the identified importance of sulfur species in ROX reduction, the effects of dissolved sulfide ions and elemental sulfur on ROX reduction by Fe_3S_4 nanosheets were more rigorously investigated. As depicted in Fig. S5, ROX was negligibly reduced by the presence of sulfide ions or elemental sulfur in solution, ruling out the direct ROX reduction contribution from dissolved sulfide or the subsequently generated elemental sulfur produced during dissolution and reduction of the Fe_3S_4. These crucial results indicate that the ROX removal processes were mediated by the structural sulfide ions and mainly took place on the surface of the Fe_3S_4 nanosheets as opposed to reactions in the solution phase.

3.6. Proposed ROX removal mechanism by Fe_3S_4 nanosheets

Based on the integrated results of this study, we postulated the reaction pathway for ROX removal by Fe_3S_4 nanosheets (Scheme 1). ROX
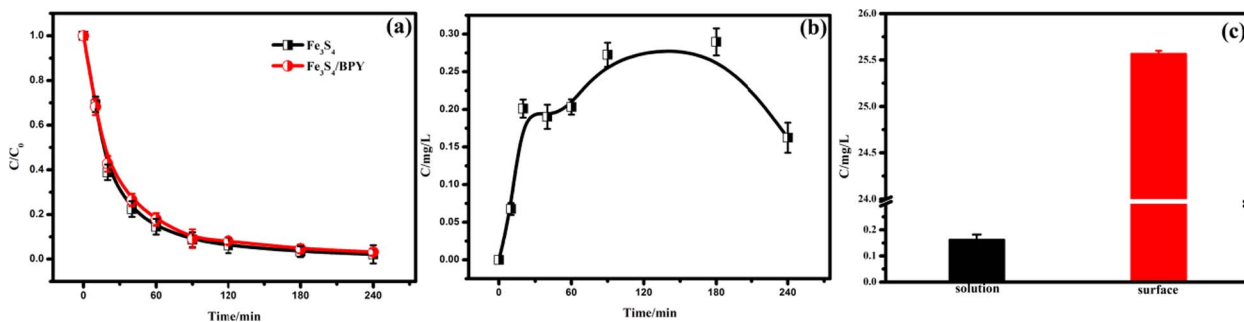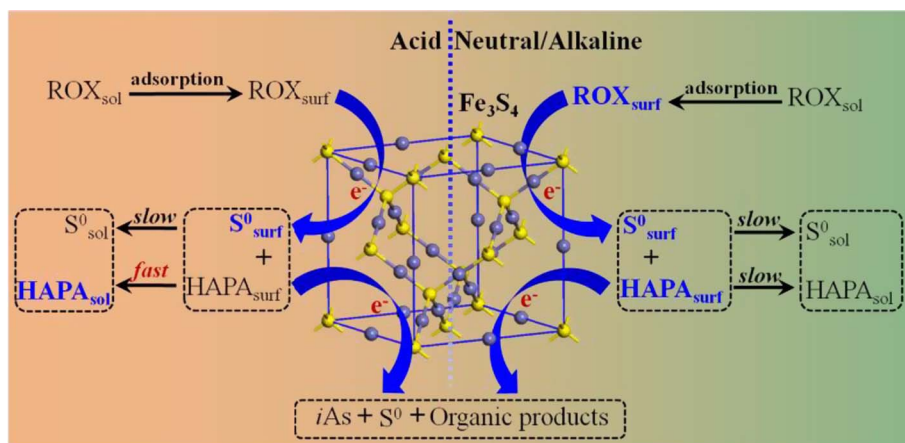

Fig. 5. (a) ROX removal efficiency in the absence and presence of BPY; (B) Time profiles of dissolved elemental sulfur generated via the oxidation of Fe_3S_4; (c) Elemental sulfur generated in solution and on the Fe_3S_4 surface during Fe_3S_4 oxidation with ROX after 240 min.

Scheme 1. The proposed ROX adsorption and reduction mechanism with magnetic Fe₃S₄.

is initially adsorbed on the surface of the Fe₃S₄ nanosheets where electrons are donated by the structural sulfide rather than the ferrous iron. The structural sulfide is oxidized to elemental sulfur instead of sulfate, sulfite or other sulfur species. This process is strongly pH dependent with a lower pH enhancing the reduction of the $-NO_2$ moiety on ROX to generate HAPA. The generated HAPA maybe subsequently desorbed from the Fe₃S₄ surface resulting in a secondary pollutant with a higher toxicity than ROX. In contrast, at neutral to alkaline pH values ROX and HAPA are preferentially adsorbed rather than reduced on the Fe₃S₄ surface. All of these reaction steps take place on the Fe₃S₄ nanosheet surface rather than in the solution phase.

4. Conclusions

In this study, ROX removal by magnetic Fe₃S₄ nanosheets was analyzed in detail. The results demonstrated that ROX was initially converted to HAPA by $-NO_2$ reduction to $-NH_2$ by structural sulfide in the Fe₃S₄ nanosheets, and then HAPA was adsorbed on the Fe₃S₄ surface, especially at neutral to alkaline pH conditions. These findings provide new insights on natural mineral-induced (e.g., iron sulfide minerals) removal of organoarsenic by sorption and redox reactions mediated by interactions with the sulfur and iron cycles.

Appendix A. Supplementary data

Supplementary data associated with this article can be found, in the online version, at http://dx.doi.org/10.1016/j.cej.2017.07.176.

References

[1] F.T. Jones, A broad view of arsenic, Poultry Sci. 86 (2007) 2–14.
[2] D.W. Rutherford, A.J. Bednar, J.R. Garbarino, R. Needham, K.W. Staver, R.L. Wershaw, Environmental fate of roxarsone in poultry litter. part II. Mobility of arsenic in soils amended with poultry litter, Environ. Sci. Technol. 37 (2003) 1515–1520.
[3] J.R. Garbarino, A.J. Bednar, D.W. Rutherford, R.S. Beyer, R.L. Wershaw, Environmental fate of roxarsone in poultry litter. I. Degradation of roxarsone during composting, Environ. Sci. Technol. 37 (2003) 1509–1514.
[4] E. D'Angelo, G. Zeigler, E.G. Beck, J. Grove, F. Sikora, Arsenic species in broiler (Gallus gallus domesticus) litter, soils, maize (Zea mays L.), and groundwater from litter-amended fields, Sci. Total Environ. 438 (2012) 286–292.
[5] B. Hileman, Arsenic in chicken production, Chem. Eng. News 85 (2007) 34–35.
[6] S. Depalma, S. Cowen, T. Hoang, H.A. Al-Abadleh, Adsorption thermodynamics of *p*-arsanilic acid on iron (oxyhydr)oxides: in-situ ATR-FTIR studies, Environ. Sci. Technol. 42 (2008) 1922–1927.
[7] J.L. Hu, Z.L. Tong, Z.H. Hu, G.W. Chen, T.H. Chen, Adsorption of roxarsone from aqueous solution by multi-walled carbon nanotubes, J. Colloid Interface Sci. 377 (2012) 355–361.
[8] J.C. Li, S.J. Yuan, W. Wang, F. Ji, Z.H. Hu, Adsorption characteristics of 4-hydroxy-3-aminophenylarsonic acid (HAPA) onto anaerobic granular sludge, Desalin. Water Treat. 1–12 (2015).
[9] D. Kong, L.D. Wilson, Synthesis and characterization of cellulose-goethite composites and their adsorption properties with roxarsone, Carbohyd. Polym. 169 (2017) 282–294.
[10] L. Poon, S. Younus, L.D. Wilson, Adsorption study of an organo-arsenical with chitosan-based sorbents, J. Colloid Interface Sci. 420 (2014) 136–144.
[11] J. Hu, Z. Tong, G. Chen, X. Zhan, Z. Hu, Adsorption of roxarsone by iron (hydr) oxide-modified multiwalled carbon nanotubes from aqueous solution and its mechanisms, Int. J. Environ. Sci. Technol. 11 (2013) 785–794.
[12] M. Tanaka, Y.S. Togo, N. Yamaguchi, Y. Takahashi, An EXAFS study on the adsorption structure of phenyl-substituted organoarsenic compounds on ferrihydrite, J. Colloid Interf. Sci. 415 (2014) 13–17.
[13] J. Tofan-Lazar, H.A. Al-Abadleh, ATR-FTIR studies on the adsorption/desorption kinetics of dimethylarsinic acid on iron–(oxyhydr)oxides, J. Phys. Chem. A 116 (2012) 1596–1604.
[14] J. Olavarría-Fullerton, S. Wells, W. Ortiz-Rivera, M.J. Sepaniak, M.A. De Jesus, Surface-enhanced raman scattering (SERS) characterization of trace organoarsenic Antimicrobials Using Silver/Polydimethylsiloxane Nanocomposites, Appl. Spectrosc. 65 (2011) 423–428.
[15] D. Lu, F. Ji, F. Wang, S. Yuan, Z.H. Hu, T. Chen, Adsorption and photocatalytic decomposition of roxarsone by TiO₂ and its mechanism, Environ. Sci. Pollut. Res. 21 (2014) 8025–8035.
[16] S. Zheng, W.J. Jiang, Y. Cai, D.D. Dionysiou, K.E. O'Shea, Adsorption and photocatalytic degradation of aromatic organoarsenic compounds in TiO₂ suspension, Catal. Today 224 (2014) 83–88.
[17] L.L. Wang, H.F. Cheng, Birnessite (δ-MnO₂) mediated degradation of organoarsenic feed additive p-arsanilic acid, Environ. Sci. Technol. 49 (2015) 3473–3481.
[18] Y.K. Liu, P. Hu, J.T. Zheng, M.B. Wu, B. Jiang, Utilization of spent aluminum for p-arsanilic acid degradation and arsenic immobilization mediated by Fe(II) under aerobic condition, Chem. Eng. J. 297 (2016) 45–54.
[19] L.Y. Wang, S.W. Wang, W.R. Chen, Roxarsone desorption from the surface of goethite by competitive anions, phosphate and hydroxide ions: significance of the presence of metal ions, Chemosphere 152 (2016) 423–430.
[20] Y.J. Wang, F. Ji, W. Wang, S.-J. Yuan, Z.-H. Hu, Removal of roxarsone from aqueous solution by Fe/La-modified montmorillonite, Desalin. Water Treat. 57 (2016) 20520–20533.
[21] B.K. Jung, J.W. Jun, Z. Hasan, S.H. Jhung, Adsorptive removal of p-arsanilic acid from water using mesoporous zeolitic imidazolate framework-8, Chem. Eng. J. 267 (2015) 9–15.
[22] M. Sarker, J.Y. Song, S.H. Jhung, Adsorption of organic arsenic acids from water over functionalized metal-organic frameworks, J. Hazard. Mater. 335 (2017) 162–169.
[23] B. Li, X.Y. Zhu, K.Y. Hu, Y.S. Li, J.F. Feng, J.L. Shi, J.L. Gu, Defect creation in metal-organic frameworks for rapid and controllable decontamination of roxarsone from aqueous solution, J. Hazard. Mater. 302 (2016) 57–64.
[24] D. Rickard, G.W. Luther, Chemistry of iron sulfides, Chem. Rev. 107 (2007) 514–562.
[25] A. Roldan, N.H. de Leeuw, Methanol formation from CO₂ catalyzed by Fe₃S₄ {111}: Formate versus hydrocarboxyl pathways, Faraday Discuss. 188 (2016) 161–180.
[26] L.M. White, R. Bhartia, G.D. Stucky, I. Kanik, M.J. Russell, Mackinawite and greigite in ancient alkaline hydrothermal chimneys: Identifying potential key catalysts for emergent life, Earth. Planet. Sci. Lett. 430 (2015) 105–114.

[27] C.B. Elizabeth, F.H. Kim, Reductive transformation of halogenated aliphatic pollutants by iron sulfide, Chem. Environ., Am. Chem. Soc. 806 (2002) 113–129.

[28] Y.Y. Gong, J.C. Tang, D.Y. Zhao, Application of iron sulfide particles for groundwater and soil remediation: A review, Water Res. 89 (2016) 309–320.

[29] H.T. Pham, K. Suto, C. Inoue, Trichloroethylene transformation in aerobic pyrite suspension: Pathways and kinetic modeling, Environ. Sci. Technol. 43 (2009) 6744–6749.

[30] Y. Bi, M. Stylo, R. Bernier-Latmani, K.F. Hayes, Rapid mobilization of noncrystalline U(IV) coupled with FeS oxidation, Environ. Sci. Technol. 50 (2016) 1403–1411.

[31] W. Liu, Y.Y. Wang, Z.H. Ai, L.Z. Zhang, Hydrothermal synthesis of FeS$_2$ as a high-efficiency Fenton reagent to degrade alachlor via superoxide-mediated Fe(II)/Fe (III) cycle, ACS Appl. Mater. Interfaces 7 (2015) 28534–28544.

[32] Q. Li, Q. Wei, W. Zuo, L. Huang, W. Luo, Q. An, V.O. Pelenovich, L. Mai, Q. Zhang, Greigite Fe$_3$S$_4$ as a new anode material for high-performance sodium-ion batteries, Chem. Sci. 8 (2017) 160–164.

[33] J. Zheng, Y. Cao, C. Cheng, C. Chen, R.W. Yan, H.X. Huai, Q.F. Dong, M.S. Zheng, C.C. Wang, Facile synthesis of Fe$_3$S$_4$ hollow spheres with high-performance for lithium-ion batteries and water treatment, J. Mater. Chem. A 2 (2014) 19882–19888.

[34] A. Roldan, N. Hollingsworth, A. Roffey, H.U. Islam, J.B.M. Goodall, C.R.A. Catlow, J.A. Darr, W. Bras, G. Sankar, K.B. Holt, G. Hogarth, N.H. de Leeuw, Bio-inspired CO$_2$ conversion by iron sulfide catalysts under sustainable conditions, Chem. Commun. 51 (2015) 7501–7504.

[35] L. Kong, L. Yan, Z. Qu, N. Yan, L. Li, β-Cyclodextrin stabilized magnetic Fe$_3$S$_4$ nanoparticles for efficient removal of Pb(II), J. Mater. Chem. A 3 (2015) 15755–15763.

[36] Z.J. Zhang, X.Y. Chen, Magnetic greigite (Fe$_3$S$_4$) nanomaterials: Shape-controlled solvothermal synthesis and their calcination conversion into hematite (α-Fe$_2$O$_3$) nanomaterials, J. Alloys Compd. 488 (2009) 339–345.

[37] W. He, H.K. Kim, W.G. Wamer, D. Melka, J.H. Callahan, J.J. Yin, Photogenerated charge carriers and reactive oxygen species in ZnO/Au hybrid nanostructures with enhanced photocatalytic and antibacterial activity, J. Am. Chem. Soc. 136 (2014) 750–757.

[38] G.V. Buxton, C.L. Greenstock, W.P. Helman, A.B. Ross, Critical review of rate constants for reactions of hydrated electrons, hydrogen atoms and hydroxyl radicals ($\cdot$OH/$\cdot$O$^-$) in aqueous solution, J. Phys. Chem. Ref. Data 17 (1988) 513–886.

[39] S.X. Ge, L.Z. Zhang, Efficient visible light driven photocatalytic removal of RhB and NO with low temperature synthesized In(OH)$_x$S$_y$ hollow nanocubes: a comparative study, Environ. Sci. Technol. 45 (2011) 3027–3033.